CFD Based Reactivity Parameter Determination for Biomass Particles of Multiple Size Ranges in High Heating Rate Devolatilization

Niko P. Niemelä[a], Henrik Tolvanen[a], Teemu Saarinen[a], Aino Leppänen[a], Tero Joronen[a,b]

[a] *Department of Chemistry and Bioengineering, Tampere University of Technology, Korkeakoulunkatu 1, 33720 Tampere, Finland*

[b] *Valmet Technologies Oy, Lentokentänkatu 11, 33900 Tampere, Finland*

Corresponding author: Niko P. Niemelä, Tel.:+358 40 838 14 34, E-mail address: niko.p.niemela@tut.fi

Abstract

This work presents a Computational Fluid Dynamics (CFD) based approach for determining the global reaction kinetics of high heating rate biomass devolatilization. Three particle size ranges of woody biomass are analyzed: small (SF), medium (MF) and large (LF) size fractions. Devolatilization mass loss is measured for each size fraction in a laminar Drop-Tube Reactor (DTR) in nitrogen atmosphere, using two nominal reactor temperatures of 873 K and 1173 K. The Single First Order Reaction (SFOR) kinetics are determined by coupling an optimization routine with CFD models of the DTR. The global pre-exponential factors and activation energies for the SF, MF and LF particles are 5 880 1/s and 42.7 kJ/mol, 48.1 1/s and 20.2 kJ/mol, and 102 1/s and 24.8 kJ/mol, respectively. The parameters are optimized for the isothermal heat transfer model in CFD programs and can be used to predict the mass loss of both small thermally thin and large thermally thick wood particles. The work demonstrates that the CFD based approach accurately characterizes the very short time scales of the high heating rate devolatilization process and is therefore suitable for solid fuel kinetic studies.

Keywords:
Computational Fluid Dynamics (CFD), Biomass, High heating rate, Pyrolysis, Devolatilization, Single First Order Reaction (SFOR)

1. Introduction

High heating rate devolatilization is an integral step in many biomass conversion technologies, such as pyrolysis reactors, gasifiers, and different combustion technologies. In devolatilization, the heated biomass undergoes a rapid degradation process to form gases, condensable vapors (tar), and solid char from the initial raw material, which in case of lignocellulosic biomass consist mainly of three biopolymers: hemicellulose, cellulose, and lignin. The devolatilization products can be further collected and processed into synthetic gas or pyrolysis oil, or utilized directly in combustion to produce heat.

From an industrial point of view, accurate estimation of the devolatilization kinetics is important in combustion system dimensioning, including the burner design and the dimensioning of the furnace. Optimization of the combustion process, such as minimizing the flue gas emissions (unburned carbon, CO and NOx), requires accurate characterization of the fuel particle's combustion properties. When the fuel properties are properly characterized, the design cost of a new combustion system can be decreased with numerical estimations, as fewer expensive full scale experiments have to be conducted.

Many computational models have been developed to describe biomass devolatilization. These models are increasingly used in Computational Fluid Dynamics (CFD) modeling, which is an important tool in the design and optimization of biomass conversion technologies. In CFD modeling, the solid fuel particles are commonly coupled with the fluid flow solution via source terms that are obtained from Lagrangian single particle calculations. The volatile release from the particles to the surrounding gas environment is calculated with a devolatilization model, usually described by global Arrhenius kinetics. Some examples of CFD studies involving particle scale biomass devolatilization modeling include [1, 2] for gasification, [3, 4] for fast pyrolysis, and [5, 6, 7] for combustion.

The complex devolatilization reactions are often combined in a single global reaction or in multiple parallel global reactions. The more advanced multiple reaction models calculate the mass loss of the biomass particles based on kinetics of different chemical groups contained in the biomass material, such as the Distributed Activation Energy Model (DAEM) reviewed in [8]. On the other hand, many authors have applied a more simplified approach and combined the large number of devolatilization reactions under a single set of Arrhenius parameters. The advantage of the simple models is that they are computationally cheap, meaning they are suitable for large scale industrial simulations. These kinds of simplified models include the

Single First Order Reaction (SFOR) model and the Two Competing Rates Kobayashi model, which are available in most commercial CFD programs such as ANSYS Fluent [9]. Kinetics for these models have been derived e.g. in [10, 11, 12].

Most of the kinetic studies for biomass devolatilization have concentrated on thermogravimetric analyzes (TGA), where the heating rate of the biomass is typically below 2 K/s. However, in industrial applications the heating rate is orders of magnitude greater, and it is well known that the biomass decomposition characteristics change when the heating rate is increased. In high heating rates, typically above 1000 K/s, the amount of volatile gases and tar products increases and the solid char fraction significantly decreases, compared to the low heating rates [13]. To obtain better information about the high heating rate kinetics, alternative experimental devices have been employed, such as heated grid apparatuses and drop-tube reactors [14, 15]. However, the increase in the heating rate typically results in a loss of controllability, as it becomes very difficult to experimentally characterize the short time scales of the particle heat up and devolatilization.

To overcome this difficulty, a CFD based optimization approach has been proposed by Simone et. al. 2009 [15] and Johansen et. al. 2016 [16]. Both studies highlight that CFD modeling offers a way for accurate characterization of the temperature-time histories of the fuel particles, which is essential for accurate kinetic modeling. In this work, the CFD based approach is extended by two main contributions: 1) accuracy of the particle temperature-time history characterization is increased by experimental particle velocity measurements, and 2) multiple particle size groups are studied in order to analyze how the particle size affects the devolatilization kinetics. The work aims to add new reference kinetics for high heating rate biomass devolatilization, as only limited data is currently available in the literature. Another aim is to present a methodology that can be useful in the characterization of the very short time scales of the high heating rate process. The kinetic parameters optimized in this work are aimed for large scale CFD simulations, and thus the relatively simple SFOR devolatilization model is used together with the isothermal heat transfer model.

A woody biomass fuel is analyzed in this work. The fuel is ground into a typical size range found in pulverized fuel applications. The fuel particles are divided into three size groups by vibrational sieving, to represent small, medium and large size fractions of the fuel. The devolatilization mass loss is measured for each size group in a high heating rate Drop-Tube Reactor (DTR) in an inert N_2 atmosphere and in two nominal reactor temperatures of 873 K and 1173 K. The particle velocity profiles are measured with an

optical method in order to validate the residence times in DTR simulations. The kinetic parameters for the SFOR model are optimized by coupling an optimization routine with ANSYS Fluent 14.5 CFD program [9], and the error between computational results and experimental data is minimized. The optimized kinetic parameters are compared with other high heating rate results found in the literature, and the effects of particle size on the parameters is discussed.

2. Methodology

Fig. 1 presents the methodology of the work. The experimental work consists of two parts: 1) fuel characterization, and 2) high heating rate mass loss studies in the DTR. The fuel characterization provides the particle properties for CFD modeling, while the mass loss data is used in the kinetic parameter optimization. Experimental data from the DTR is collected during measurements to be used for boundary conditions, validation data, and drag law evaluation in the CFD modeling.

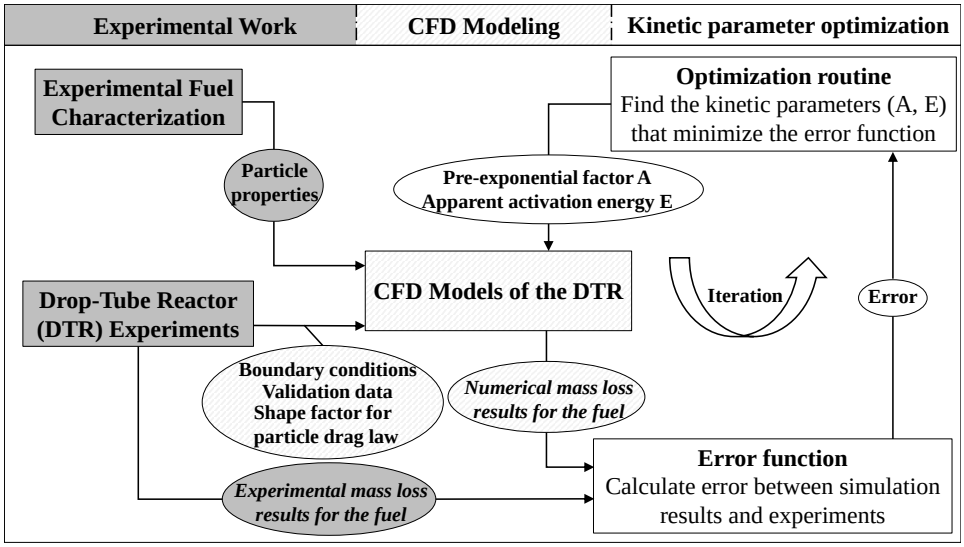

Figure 1: Optimization routine for the kinetic parameters.

A separate CFD model of the DTR is constructed for each experimental test condition in order to account the external particle conditions as accurately as possible in the kinetic parameter optimization. The temperature and flow fields of the simulations are validated with comparison to

experimental data. A great effort is made to accurately characterize the external temperature and flow conditions, particle size distributions, particle residence times, and thermophysical particle properties in the CFD models.

An optimization routine in MATLAB R2015a [17] is coupled with the CFD models of the DTR. The kinetic parameters are optimized to minimize the error between the simulation results and the experimental mass loss data. The optimization is conducted separately for three particle size groups of the biomass fuel in order to analyze the effects of particle size on the kinetic parameters. In addition, the aim is to obtain kinetic parameters that can describe the devolatilization of the whole size distribution of the fuel in large scale CFD simulations.

3. Experimental Work

3.1. Fuel Characterization

The woody biomass is ground and sieved, and three size fractions are taken to further analysis:

1. Small size fraction (SF): sieving size 112-125 µm
2. Medium size fraction (MF): sieving size 500-600 µm
3. Large size fraction (LF): sieving size 800-1000 µm.

Furthermore, the fuel is characterized by the following measurements:

1. Ultimate and proximate analysis
2. Volume-equivalent spherical diameter distributions
3. Particle density measurement
4. Mass loss measurements in a Drop-Tube Reactor (DTR)
5. Particle velocity measurements in the DTR

The experimental work is presented in more detail in the following sections.

3.1.1. Ultimate and Proximate Analysis

The ultimate and proximate analysis have been measured in a commercial research laboratory according to standardized methods. The results are presented in Table 1.

Table 1: Ultimate and proximate analyzes, wt-% dry basis

Ultimate Analysis		Proximate Analysis	
C	49.4	Volatile matter	84.1
O (calculated)	43.1	Char (by difference)	15.1
H	6.2	Ash (815°C)	0.8
N	<0.1	LHV (MJ/kg)	18.36
		Bulk Density (kg/m^3)	540

3.1.2. Size Distributions of the Sieved Fractions

Volume-equivalent spherical diameter distributions are measured for each of the three size fractions (SF, MF, LF). The spherical diameters are determined with a particle imaging software, using projections of the particles for calculating the volume-equivalent spheres. The method is presented in more detail in references [18, 19].

Each size distribution is further discretized into 10 volume fractions, each containing 10% of the total volume. A volume-mean diameter is calculated for the 10 volume fractions to be further used in the kinetic parameter optimization. Using this distributed diameter approach, the different behavior of particles of different size is better resolved if compared to a single mean diameter approach, as discussed in [15, 20, 21]. The size distributions and mean diameters are presented in Fig. 2 and Table 2, respectively. As the results indicate, the spherical volume-equivalent diameters are considerably larger than the sieving dimensions. This is because some large volume particles have a large aspect ratio and thus fit through the sieves when they are suitably aligned.

3.1.3. Density Measurement

The density of the fuel particles is measured with a mercury porosimeter, which is based on a mercury intrusion method. From the porosimeter results, the particle density has been calculated as a function of pore size in between the particles and the particle surface, as presented in Fig. 3. As the figure indicates, the porosimeter results are well in line with the bulk density value presented in Table 1.

The goal of the density measurement is to approximate the particle density such that the volume-equivalent spherical particles, presented in Table 2, contain the same solid mass as the real elongated biomass particles. This ensures that the volume-equivalent diameters also represent mass-equivalent particles in the numerical modeling. As seen in Fig. 3, at the pore size of 13 µm a clear shoulder exists in the density curve. This can be identified as a

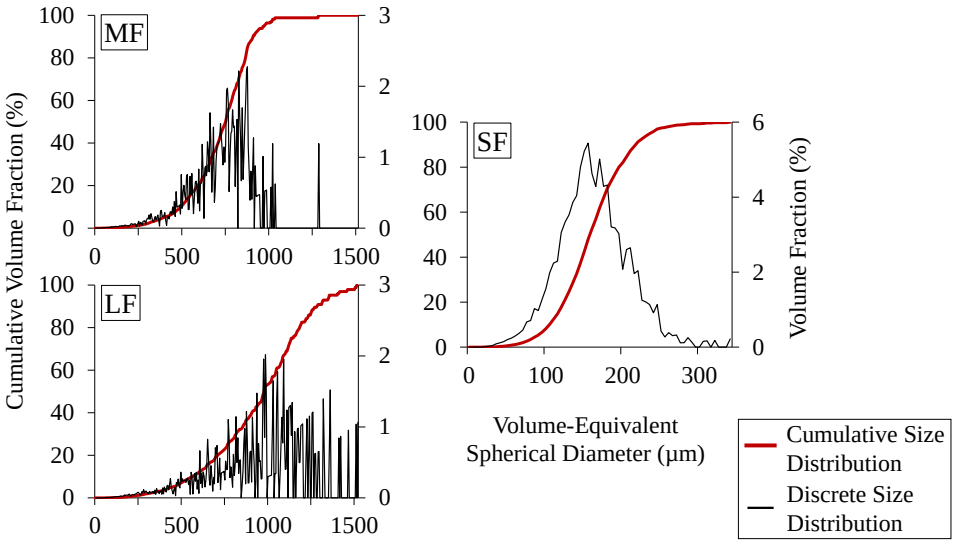

Figure 2: The volume-equivalent spherical size distributions of SF, MF and LF.

Table 2: Discretized size distributions of SF, MF and LF.

Cumulative Volume Range (%)	Volume-mean Diameter (µm)		
	SF	MF	LF
0-10	93.1	397.8	444.8
10-20	120.4	547.0	649.3
20-30	135.5	633.1	771.0
30-40	147.3	684.0	871.5
40-50	157.3	728.4	962.4
50-60	167.6	766.3	1021.3
60-70	178.1	806.5	1087.3
70-80	191.9	848.6	1139.6
80-90	210.8	879.8	1234.5
90-100	241.0	969.1	1358.2

threshold pore size, where the mercury has filled the external space between the fuel particles and starts to fill the pores in the particle surface. The density corresponding to this pore size is defined as the envelope particle density (900 kg/m^3). However, the pictures of the particle imaging software were analyzed and it was noticed that some external volume has been included in the spherical diameters due to insufficient camera resolution. A

slightly higher pore diameter of 36 µm is therefore chosen as a threshold value for the particle density (700 kg/m^3). This value is presumed to better describe the mass-equivalent spherical particles, but a more precise method should be developed in the future.

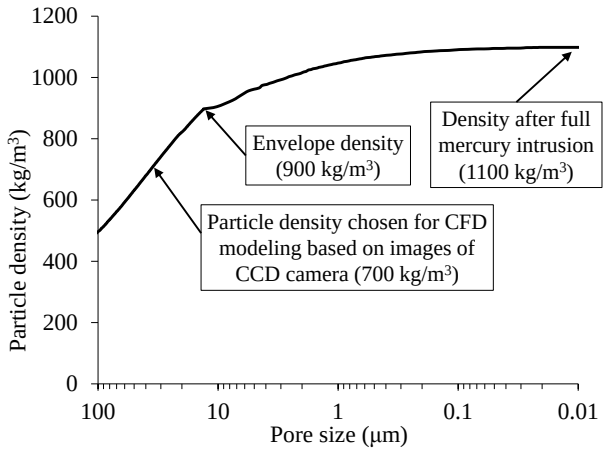

Figure 3: Density evaluation from the mercury porosimeter data. Different definitions for the particle density are displayed.

3.2. Drop-Tube Reactor (DTR) Experiments

The DTR is electrically heated and it has maximum and minimum drop distances of 67.5 cm and 5.5 cm, respectively. It has a liquid nitrogen cooled collection vessel, where the dropped particle samples are collected and quickly cooled in order to stop any chemical reactions. There are two windows at the sides of the reactor to allow visual access inside the reactor. The test device is used in two types of measurements. First, the particle velocities are measured in the 873 K nominal reactor temperature with a system consisting of a high speed CCD camera, a light pulsation device, and an image analysis program. The velocity measurement is based on producing two particle shadows in the CCD camera pictures with the light pulsation device. The particle velocities are then calculated using the distance between the two shadows and the time delay of the light pulses. Full details of the system can be found in references [18, 19]. The results from the particle velocity measurements are presented in Section 5.1.

In the second experiments, the mass loss of the three size fractions is measured as a function of drop distance in N_2 atmosphere using two nominal reactor temperatures of 873 K and 1173 K. The samples are oven-dried

before the experiments. The mass loss measurements are based on the assumption that all particles can be collected in the collection vessel. Thus, the mass loss is calculated by weighing the fuel samples before and after they are dropped through the reactor. The ability to collect all particles has been validated with cold reactor tests. In addition, it has been observed through the measurement window and from the particle impact points on the collection vessel, that the particles fall effectively close to the centerline of the reactor and do not spread on the reactor walls. This further indicates that the particles are effectively collected. A full description of the test device, as well as of the mass loss measurement procedure can be found in references [18, 19].

The experimental mass loss data for each size fraction is presented in Table 3. At least two mass loss samples were collected from each drop distance and the standard deviation is included in Table 3. At the lower reactor temperature there is a slightly higher standard deviation in the first three experimental data points of the SF size fraction. In general, however, the experimental results are very consistent. A rather high number of experimental data points is used in the optimization, which is expected to reduce the error caused by individual data points.

4. Numerical Modeling

4.1. CFD Models of the DTR

A CFD model of the DTR is constructed for each experimental drop distance reported in Table 3. Separate CFD models are made in order to account the different wall temperature profiles of each drop distance, and thus to accurately describe the external flow and temperature conditions for the particles. A schematic figure of the computational domain is presented in Fig. 4. The modeling is conducted with 3-dimensional reactor models, and the meshes contain approximately 600 000 hexahedral cells. The grid independence has been examined with one of the CFD models and presented in reference [22].

The walls of the particle feeding probe are modeled as constant temperature boundaries, justified by the water cooling inside the probe. The connector pipes of the measurement windows are simplified as constant temperature boundaries. The glass windows are modeled with a conductive and radiative boundary condition, being semi-transparent for radiation. The reactor wall temperature is based on measurements and is specific for each drop distance. An example profile for the reactor temperature of 873 K and drop distance of 19.5 cm is presented in Fig. 4.

Table 3: Experimental mass loss data including corrected sample standard deviation. The number of samples in shown in parenthesis.

Drop Distance (cm)	Mass Loss in 873 K (wt-%, db)	Mass Loss in 1173 K (wt-%, db)
Small Fraction (SF)		
5.0	-	28.3±3.2 (3)
7.5	-	63.8±1.5 (2)
9.5	-	84.7±2.8 (3)
11.5	21.6±8.2 (5)	-
13.5	-	94.1±1.4 (3)
15.5	32.9±11.5 (4)	-
17.5	56.3±6.4 (3)	95.0±0.7 (3)
19.5	63.2±2.5 (3)	-
25.5	71.2±1.7 (3)	-
Medium Fraction (MF)		
17.5	-	2.7±0.7 (2)
32.5	-	22.1±3.5 (2)
35.5	3.7±1.6 (3)	-
47.5	12.1±2.0 (3)	49.6±4.0 (2)
57.5	16.4±1.8 (3)	-
67.5	25.5±3.9 (3)	65.7±2.0 (2)
Large Fraction (LF)		
17.5	-	0.4±0.7 (3)
32.5	-	14.4±3.9 (3)
35.5	0.8±0.06 (3)	-
47.5	5.7±1.1 (3)	25.5±0.5 (2)
57.5	8.1±1.3 (3)	-
67.5	15.3±1.7 (3)	43.2±6.1 (2)

The primary and secondary gas inlets are modeled with a mass-flow inlet condition. Laminar flow equations are used, justified by the low Reynolds numbers used in the experiments. Thus, no turbulence closure model is required. The gravity is included in the modeling and the outlet boundary is kept in atmospheric pressure. The radiation is modeled with the Discrete Ordinates (DO) model and the nitrogen atmosphere is assumed non-absorbing for the radiation. The specific heat capacity, thermal conductivity, and viscosity of nitrogen are calculated with the temperature dependent polynomial functions available in Fluent database. Steady state equations are used.

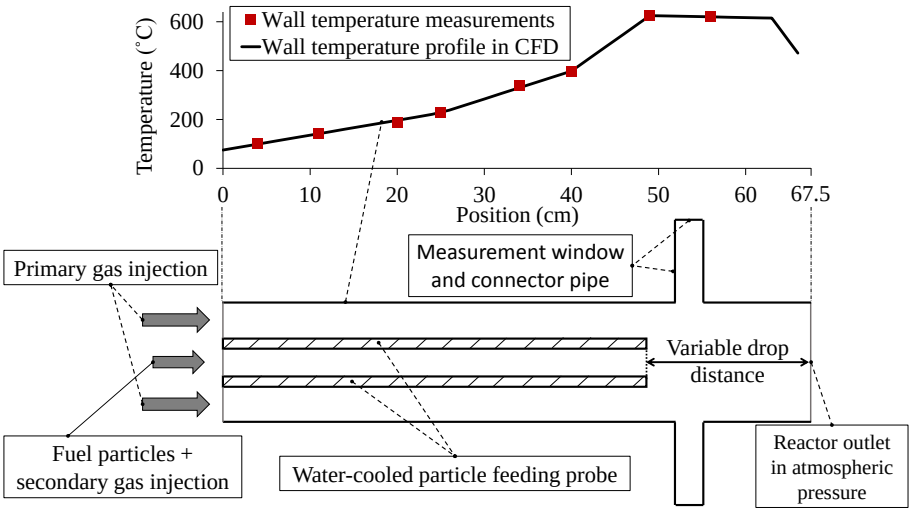

Figure 4: Cross section of the computational domain. A reactor model and wall temperature profile is constructed for each separate drop distance. The temperature at the end of reactor wall decreases, because no heating elements exist at the final 2.5 cm.

The temperature field of the simulations is validated with additional thermocouple simulations. The thermocouple, used for measuring the reactor centerline temperature, did not have a radiation cover and the measurements could not be directly compared with the simulated gas temperature. Thus, conjugate heat transfer simulations including the thermocouple inside the reactor were conducted. The thermocouple head temperature from the simulations was then compared with the measurements, as presented in Fig. 5. The validation simulations are presented in more detail in reference [22].

The velocity field of the simulations is validated by comparing the gas velocity at the reactor centerline with the experimental velocity data of the smallest particle size group (SF). Fig. 5 presents the results from this analysis. The figure indicates that the gas and the particle velocity profiles have remarkably similar shapes and the slip velocity remains approximately constant throughout the centerline profile. Based on these observations, the CFD model is considered accurate and used further in the optimization of the kinetic parameters.

4.2. Particle Modeling

The fuel particle movement inside the DTR is modeled in the Lagrangian reference frame with the Discrete Phase Model (DPM) in Ansys Fluent

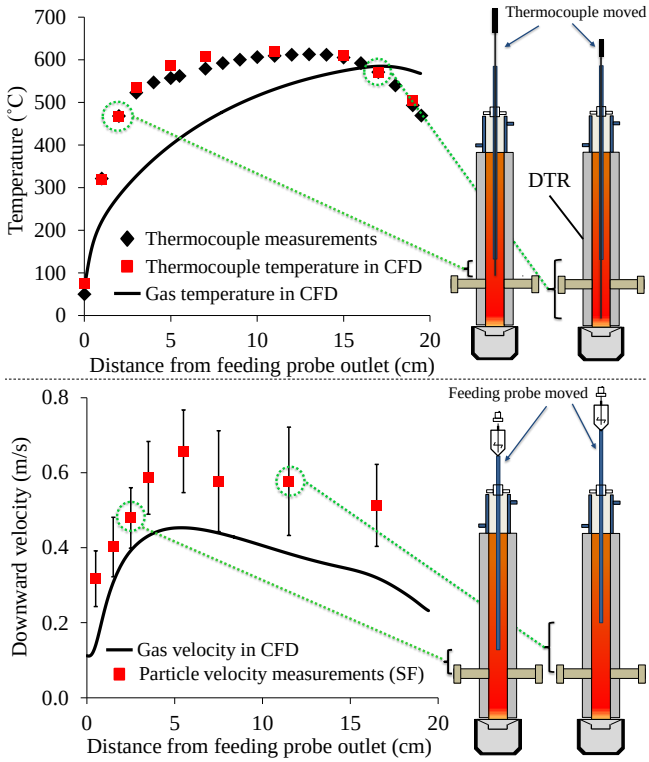

Figure 5: Validation results for the CFD model of the DTR.

14.5. The particle velocity and position in the fluid flow are solved by integrating the force balance on the particles, which includes the gravity and the drag force between the particles and the surrounding gas. The particle trajectory calculations are coupled with the heat transfer model, which takes into account the convective and radiative heat transfer on the particles. During heat up, the particles lose their mass according to the SFOR devolatilization model.

The particle modeling is conducted with one-way coupling, i.e. the flow and temperature fields inside the reactor are kept constant during the particle calculations. This is justified by the low particle feeding rate, as the particles and volatile gases presumably have an insignificant effect on the steady state conditions inside the reactor. The equations and particle properties relevant for this work are presented in the following sections. Detailed information on the Lagrangian particle modeling can be found from various sources, see for example the ANSYS Fluent theory guide [23].

4.2.1. Drag Law

The drag force per unit particle mass is solved from the following equation

$$\vec{f_D} = \frac{18\mu}{\rho_p d_p^2} \frac{C_D Re_p}{24} (\vec{u} - \vec{u_p}), \tag{1}$$

where μ ($\mathrm{kgm^{-1}s^{-1}}$) is the dynamic viscosity of the fluid, d_p (m) the spherical particle diameter, C_D (-) the drag coefficient, $Re_p = \rho d_p \left|\vec{u_p} - \vec{u}\right| / \mu$ the particle Reynolds number, $\vec{u_p}$ ($\mathrm{ms^{-1}}$) the particle velocity vector, and $\vec{u}$ ($\mathrm{ms^{-1}}$) the surrounding gas velocity. In this work, the non-spherical drag law of Haider and Levenspiel [24] is used for the drag coefficient because of the elongated shape of the biomass particles. The drag coefficient C_D is obtained from

$$C_D = \frac{24}{Re_p} \left(1 + b_1 Re_p^{b_2}\right) + \frac{b_3 Re_p}{b_4 + Re_p}, \tag{2}$$

where b_1, b_2, b_3, b_4 (-) are functions of the shape factor ϕ (-), which is defined as

$$\phi = \frac{A_p}{A_{act}}, \tag{3}$$

where A_p ($\mathrm{m^2}$) is the surface area of the spherical volume-equivalent particle and A_{act} ($\mathrm{m^2}$) is the actual surface area of the particle. In this work, a suitable shape factor is determined such that the particle velocities in CFD simulations correspond with the experimental measurements. At the same time, the ability of the non-spherical drag law to describe the biomass particles' velocities is evaluated. The suitable shape factor and the corresponding particle velocity profiles are presented in Section 5.1.

4.2.2. Heat Transfer

The particle temperature-time histories are solved from the heat balance equation:

$$m_p c_p \frac{dT_p}{dt} = h A_p (T_\infty - T_p) + \epsilon_p A_p \sigma (\Theta_R^4 - T_p^4), \tag{4}$$

where m_p (kg) is the particle mass, c_p ($\mathrm{Jkg^{-1}K^{-1}}$) the specific heat capacity, h ($\mathrm{Wm^{-2}K^{-1}}$) the convective heat transfer coefficient, A_p ($\mathrm{m^2}$) the particle surface area, T_∞ (K) the surrounding gas temperature, T_p (K) the particle temperature, ϵ_p (-) the particle surface emissivity (0.9 in this work as Fluent default), σ the Stefan-Boltzmann constant, $\Theta_R = (G/4\sigma)^{1/4}$ (K) the radiation temperature, and G ($\mathrm{Wm^{-2}}$) the incident radiation from the reactor

walls on the particle surface (obtained from the numerical radiation solution in the CFD model). The convective heat transfer coefficient h is calculated from the correlation of Ranz and Marshall [25]. The heat of the pyrolysis reactions is not included in Eq. 4, as in a high heating rate device it is negligible compared to the heat transport from the particle surroundings. In order to solve the particle temperature T_p, Eq. 4 is integrated over discrete time-steps and solved in conjunction with the Lagrangian particle trajectory calculations.

A value of $c_p = 1500$ Jkg^{-1}K^{-1} is used for the specific heat capacity of the dry wood particles. It is emphasized that the c_p is strongly coupled with the optimized kinetic parameters, because the specific heat capacity determines the particle temperature which in turn determines the rate constant of the devolatilization model. Whenever the kinetic parameters obtained in this work are used in CFD simulations, it is recommended that the same c_p is used for the wood particles. Based on optimization tests, multiple specific heat capacity values can produce identically good fit to the experimental data. The different kinetic parameters only function with the specific heat capacity they have been optimized with.

It is important to note here that the particles are considered isothermal, meaning that the heat travels infinitely fast inside the particles resulting in a uniform temperature throughout the volume. In a high heating rate device, such as the DTR of this work, the internal heat transfer resistance may become significant even for sufficiently small particles. In this work, all particles are modeled as isothermal spheres, which is a major simplification. In reality, the studied biomass particles are of multiple different shapes and the large particles belong evidently in the thermally thick particle size regime. However, as discussed in [26] the combination of isothermal approach and global reactivity parameters can predict realistic devolatilization times, because the kinetic parameters can compensate the error made by the assumptions. The global reactivity parameters can be viewed as parameters that absorb the effects of complex chemical reactions, but also compensate the effects of internal heat transfer resistance. This approach is applied for two main reasons, firstly compatibility with the commercial CFD programs and the isothermal particle models is maintained, and secondly the computational demand is not increased because no additional internal heat transfer calculations are required. These factors are of high importance in large scale industrial CFD simulations.

4.2.3. Mass Loss in Devolatilization

The initial particles consist of fixed mass fractions of volatiles, char and ash. The devolatilization reactions are combined in one global reaction:

$$\text{particle (s)} \xrightarrow{k} \text{volatiles (g)}. \tag{5}$$

After the predetermined mass fraction of volatiles has escaped from the particles, only char and ash remain. In full scale CFD modeling, the composition of the volatiles in Eq. 5 can be further defined by the modeler and the subsequent chemical reactions described by an appropriate reaction scheme. In this work, no further modeling for the volatiles is required because of the one-way coupling between the particles and the surrounding gas phase. The mass loss rate of volatiles to the surrounding gas atmosphere is calculated with the Single First Order Reaction (SFOR) model. It assumes that the devolatilization rate is first-order dependent on the amount of volatiles remaining in the particle:

$$-\frac{dm_p}{dt} = k[m_p - (1 - f_{v,0})m_{p,0}], \tag{6}$$

where k (s^{-1}) is the global rate constant of the devolatilization reactions, $f_{v,0}$ (-) the initial mass fraction of volatiles in the particle, and $m_{p,0}$ (kg) the initial particle mass. The rate constant k is calculated via Arrhenius equation:

$$k = Ae^{-(E/R_u T_p)}, \tag{7}$$

where A (s^{-1}) is the pre-exponential factor, E (Jmol^{-1}) the apparent activation energy, and R_u ($\mathrm{Jmol}^{-1}\mathrm{K}^{-1}$) the universal gas constant. The aim of the kinetic parameter optimization is to define A, E and $f_{v,0}$, so that the error between the simulation results and the experimental mass loss data is minimized.

As the particle loses its mass, the particle diameter changes according to a swelling coefficient C_{sw}, see [23] for further details. A value of $C_{sw} = 0.9$ is used based on the observations made in [19]. This means that the particle diameter is 90% of the initial diameter when the devolatilization terminates.

4.3. Optimization of the Kinetic Parameters

The kinetic parameters, A and E in Eq. 7, are optimized separately for each size fraction (SF, MF, LF) with an unconstrained nonlinear optimization routine. The algorithm is based on the simplex search method of Lagarias et al. [27], which searches the minimum for a function without

numerical or analytic gradients. In this work, the MATLAB optimization algorithm is coupled directly to the ANSYS Fluent 14.5 software using Fluent as a Server connection. The optimization algorithm is designed to minimize an error function, which calculates the error between the simulation results and the experimental mass loss data through a sum of squared residuals:

$$\text{error} = \sum_{i=1}^{j} (X_{exp,i} - X_{sim,i})^2, \tag{8}$$

where j is the number of drop distances for the size group, $X_{exp,i}$ is the experimental mass loss for drop distance i, and $X_{sim,i}$ is the calculated mass loss for drop distance i (the drop distances are presented in Table 3). The optimization is conducted simultaneously for both nominal reactor temperatures in order to obtain kinetic parameters that function in the whole temperature interval being studied.

The numerical mass loss $X_{sim,i}$ is obtained from the CFD models by injecting the ten discrete particle diameters (see Table 2) through the reactor. For each drop distance i, the mass loss is obtained through a mass-weighted average:

$$X_{sim,i} = \sum_{k=1}^{10} f_k x_k, \tag{9}$$

where $f_k = 0.10$ is the mass fraction of each discrete diameter k, and x_k is the mass loss of diameter k at the reactor outlet. Each particle is injected into the reactor from the center point of the feeding probe inlet, as the injection position had no significant contribution to the particle mass loss.

The particle properties described in the previous sections are preset into the CFD models, thus only variables the optimization algorithm has to change are the kinetic parameters A and E, and the fixed volatile yields $f_{v,0}$ for the two nominal reactor temperatures. The volatile yields are optimized only for the smallest size group SF, because this is the only fraction having experimental data from the final parts of the conversion curves (see Table 3). The same volatile yields are used for the MF and LF size groups, because the optimization algorithm had difficulties in optimizing the volatile yields due to lack of experimental data from the final conversion levels.

5. Results and Discussion

5.1. Particle Velocity Profiles

The shape factor ϕ in the non-spherical drag law of Haider and Levenspiel [24] determines the drag coefficient in Eq. 2 and significantly affects the

particle velocities and the resulting residence times in CFD modeling. The shape factor was carefully determined based on the velocity measurements before the optimization routine was conducted.

Fig. 6 presents the CFD calculated velocity profiles for each size fraction, along with their measured velocities, at the nominal reactor temperature of 873 K. In this lower reactor temperature, the kinetic parameters did not have a significant effect on the particle velocity profiles, which enabled the determination of the shape factor before the final parameters were optimized. The profiles in Fig. 6, however, are calculated with the final optimized parameters. The most suitable shape factor was concluded to be $\phi = 0.25$ for all size fractions, which is a very reasonable value to represent the ratio of the volume-equivalent spheres' area to the real surface area of the biomass particles.

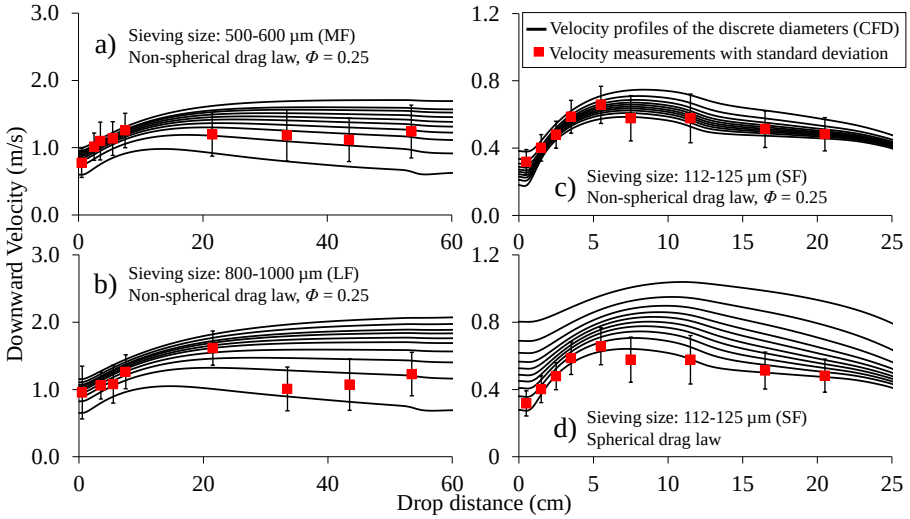

Figure 6: CFD calculated velocity profiles for each size fraction, along with their measured velocities, at the nominal reactor temperature of 873 K. Graphs a), b) and c) display the profiles used in the kinetic parameter optimization. Graph c) demonstrates how the spherical drag law is not suitable for these biomass particles.

The small particle SF data was most extensive, and thus it was used as a main data set to determine the shape factor. As seen in Fig. 6, the calculated SF velocity profiles go very accurately through the experimental measurements when the nonspherical drag law is used (graph c). Furthermore, the scatter of the discrete diameters is well within the measured standard deviations. The non-spherical drag law describes the particle velocities with detailed accuracy and it was concluded to be a suitable model for the small

biomass particles. As the graph d) indicates, the spherical drag law could not describe the experimental SF velocities.

As seen in the graphs a) and b) of Fig. 6, the MF and LF particles have slightly worse correlation with the experimental data, compared to the SF particles. This is mostly explained by the limited data, as time constraints did not allow for more comprehensive measurements. More data should be collected in the future studies in order to improve shape factor determination for the larger size fractions. Considering the experimental uncertainties, the shape factor $\phi = 0.25$ was considered the most suitable also for the MF and LF size fractions. As with the SF particles, the spherical drag law could not describe the experimental MF/LF velocities.

5.2. Optimization Results

The optimized kinetic parameters for the three size fractions are presented in Table 4. For the smallest size fraction (SF), the volatile yield $f_{v,0}$ (db) was kept as a variable during optimization. The same volatile yields were used for the MF and LF particles, as with these particles no experimental data was obtained from the final conversion levels (see Table 3) because of insufficient DTR length. In reality, the volatile yields of MF and LF fractions may be slightly lower compared to the small particles, because the larger size may result in higher char formation. Asadullah et al. [28] have studied the effect of particle size on a woody biomass char yield in similar high heating rate conditions (>1000 K/s, 1173 K reactor temperature) and obtained char yields of approximately 4% and 5% for average diameters of 300 µm and 800 µm, respectively. Based on their study, the difference between the MF/LF and SF volatile yields is expected to be small. For completeness, however, the DTR should be modified such that the final volatile yields could be measured also for the larger biomass particles. The SF volatile yield in the lower reactor temperature should be validated with an additional measurement point from a higher drop distance.

When the kinetic parameters in Table 4 are compared, it is noticed that the MF and LF particles have significantly smaller pre-exponential factors A and activation energies E compared to the SF parameters. The MF and LF parameters, however, are very similar which is reasonable as both size groups belong evidently in the thermally thick particle size regime and have partly overlapping size distributions. The MF and LF parameters are optimized based on their own separate mass loss and particle size distribution measurements, thus the highly similar reactivity parameters demonstrate the consistency of the presented methodology.

Table 4: Optimized kinetic parameters for the three size fractions, as well as the common particle properties to be used with the kinetics.

	SF (112-125 µm)	MF (500-600 µm)	LF (800-1000 µm)
A (1/s)	5 880	48.1	102
E (J/mol)	42 720	20 212	24 784
$f_{v,0}$(873 K) (%)	76.1	SF value	SF value
$f_{v,0}$(1173 K) (%)	94.2	SF value	SF value
Common particle properties			
Density (kg/m^3)		700	
Specific heat capacity (kJ/kgK)		1500	
Shape factor for drag law (-)		0.25	

Fig. 7 compares the experimental and CFD mass loss results from the studied drop distances. For each data point, the particles have distinct temperature-time histories depending on the feeding probe position and reactor wall temperature profile, which is the reason why the conversion curves are not presented as single lines. The mean absolute error between the calculated and experimental results is below 2.5 percentage units for all particle size fractions. It can be concluded that the optimized parameters are able to describe the experimental data with a good accuracy in both temperature levels. The results indicate that the SFOR model can successfully describe the mass loss of the biomass particles, despite of the high number of reactions it incorporates in the single kinetic parameters.

5.3. Comparison of the Kinetic Parameters

Fig. 8 presents the mass loss, the particle temperature, and the particle heating rate as a function of residence time for the mass-mean particles of the three size fractions. The figure is constructed by simulating the particle trajectories in an extended model of the DTR in order to produce the complete conversion curves of the larger particles. Fig. 8 demonstrates that the smallest particles heat up and devolatilize significantly faster than the medium and large particles, which is reasonable as the MF and LF particles have 87 and 197 times the mass of the SF particle, respectively. With all particle sizes, the time required for complete devolatilization is comparable to the time required to heat up the particles up to the reactor temperature. As an example, with the SF particle in the 1173 K nominal reactor temperature, a significant mass loss starts at around 500 K, the devolatilization terminates at 1060 K, and the highest mass loss rate occurs at 900 K particle

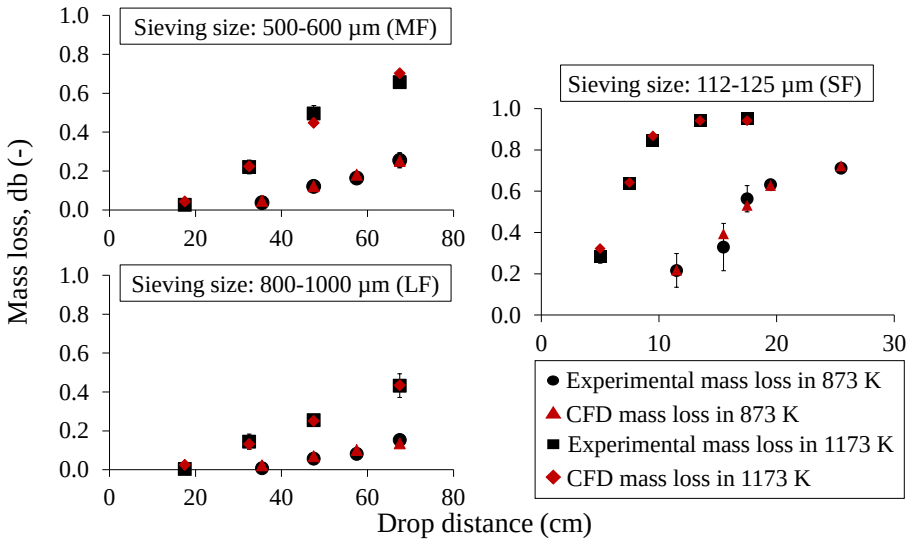

Figure 7: CFD simulation results obtained with the optimized kinetic parameters and compared with the experimental mass loss data introduced in Table 3.

temperature. Thus, the devolatilization occurs in a wide temperature range and most of the mass loss has already occurred before the particles reach the nominal reactor temperature.

The optimized kinetic parameters of the LF and MF fractions are very similar, as was concluded from Table 4. However, Fig. 8 indicates that the two parameters result in different mass loss behavior at the final parts of the conversion curves (above 60% conversion). At high particle temperatures, the MF kinetics predict a slightly slower reaction rate compared to the LF kinetics. This deviation is most probably caused by the lack of experimental data from the final conversion levels, combined with the experimental errors in the mass loss data used in the optimization. The similar conversion curves indicate that the devolatilization of MF and LF particles is possibly described by the same global kinetics. The similar global reactivity can be explained by a similar internal heat transfer resistance, as in case of this fuel the increase in particle size mainly results in more elongated particles rather than more thick ones.

The three reactivity parameters are further compared in the Arrhenius plot of Fig. 9 (left). The Arrhenius plot shows that the SF kinetics deviate significantly from the MF and LF kinetics, while the latter two are very close to each other. The obtained kinetics can be clearly divided into two categories, where the small particles are described by the SF kinetics and

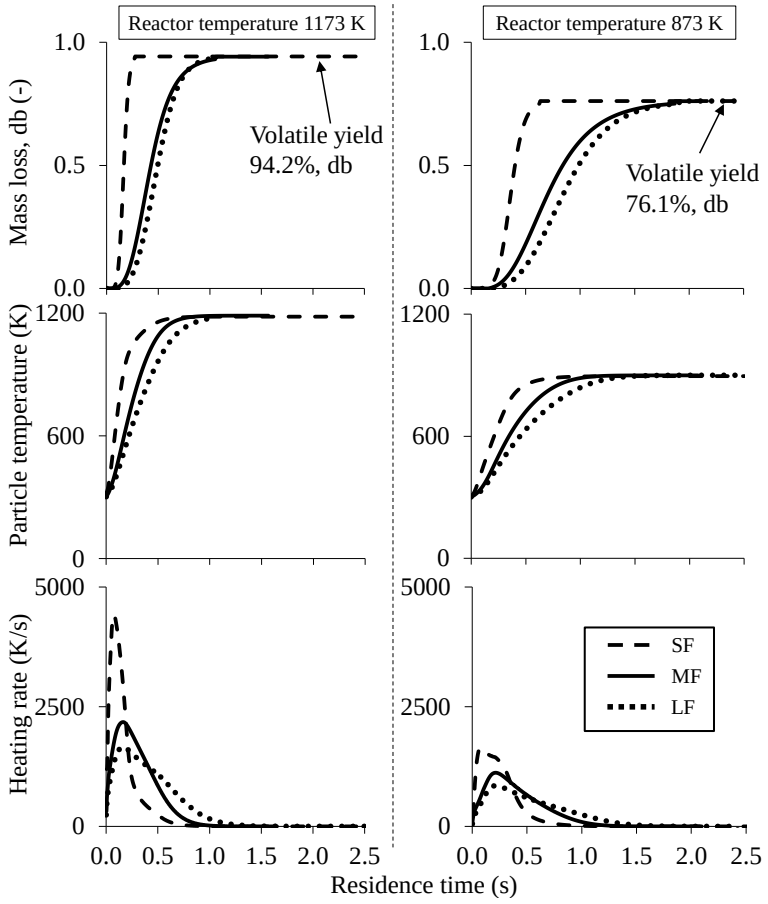

Figure 8: Mass loss, particle temperature, and heating rate as a function of residence time for the mass mean particles of the three size fractions. The particle diameters are 954 µm, 726 µm and 164 µm for LF, MF and SF, respectively. The left and right columns present the results in the reactor temperatures of 1173 K and 873 K, respectively.

the medium and large particles by either MF or LF kinetics. A logical explanation for the different kinetics is the internal heat transfer resistance of the larger particles. The MF and LF particles are modeled with the isothermal assumption which neglects the internal heat transfer resistance, and it is rationalized that the MF/LF kinetics have compensated the error that is made by this assumption. Johansen et al. [26] have derived heat transport corrected SFOR kinetics for isothermally modeled thermally thick biomass particles based on a theoretical analysis. They obtained a similar result, that the absolute gradient in the Arrhenius plot decreases as a function of

increasing particle size. It is interesting to note that this work observes the same phenomena in reactivity parameters optimized based on experimental data. From the current results, it is not clear if the difference between the SF and MF/LF kinetics is purely caused by the internal heat transfer effects or do the kinetics also change because the larger particles experience a lower heating rate than the small ones. This effect could be studied with a separate optimization where the internal heat transfer calculations are included for the large particles.

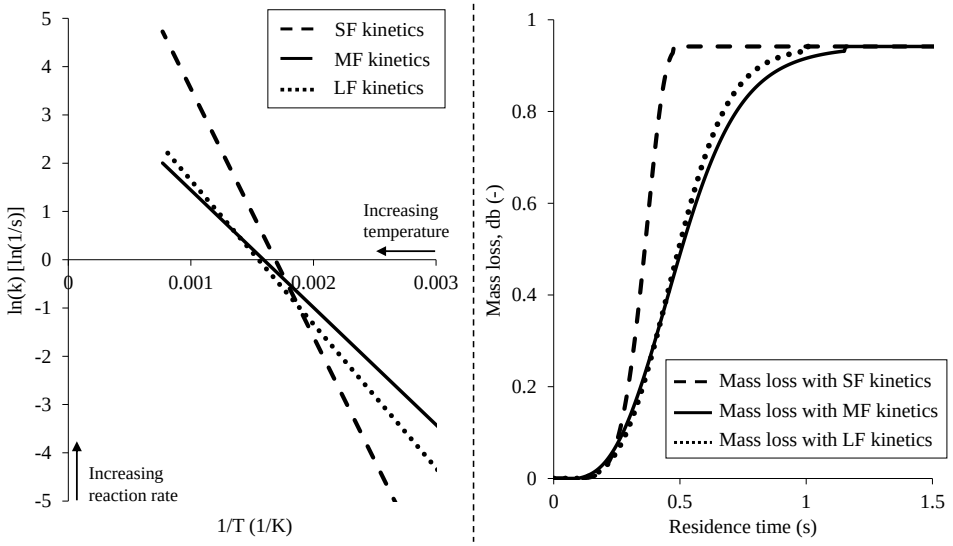

Figure 9: Left: Arrhenius plot for the kinetic parameters of SF, MF, and LF. Right: Mass loss history of the mass mean diameter of LF (954 µm) calculated with the three different kinetics in the nominal reactor temperature of 1173 K.

The graph on the right side of Fig. 9 compares the mass loss history of the LF mass mean diameter calculated with the three different kinetics in the 1173 K nominal reactor temperature. The graph further demonstrates the similarity of the MF and LF kinetics. It also demonstrates how significant the difference between the SF and MF/LF kinetics is, as the former highly underestimate the time required for full devolatilization. Considering large scale CFD simulations, it is clear that the SF kinetics cannot be used for the large thermally thick fuel particles. Because of the compensation effect of the MF/LF kinetics, it is expected that the devolatilization time of the large particles can be realistically predicted with the separately optimized kinetics, without need for modifications to the basic isothermal heat transfer model and increase in the computational time. It is expected that the MF/LF

kinetics can aid in the prediction of unburned fuel in fly ash in large scale CFD simulations.

5.4. Comparison to Other Studies

The pre-exponential factors A and the activation energies E obtained for the size fractions are in general much smaller than the values obtained from low heating rate TGA analysis, where the heating rate is typically below 2 K/s. The low heating rate activation energies for woody biomass are commonly in the range between 60-240 kJ/mol, as collected from various studies by Gronli in [29]. In high heating rate studies for various biomass materials, the reported heating rates are typically of the order of 1000 K/s, and the activation energies lie in the range between 21-74 kJ/mol [11, 14, 15, 16]. A low activation energy is a consistent result in high heating rate studies, but to the authors' knowledge no comprehensive explanation has been provided. It is possible that different decomposition reactions may become dominant when the heating rate of the material is increased. Johansen et al. [16] have demonstrated that the low heating rate kinetics are poorly suited for CFD simulation of a high heating rate device.

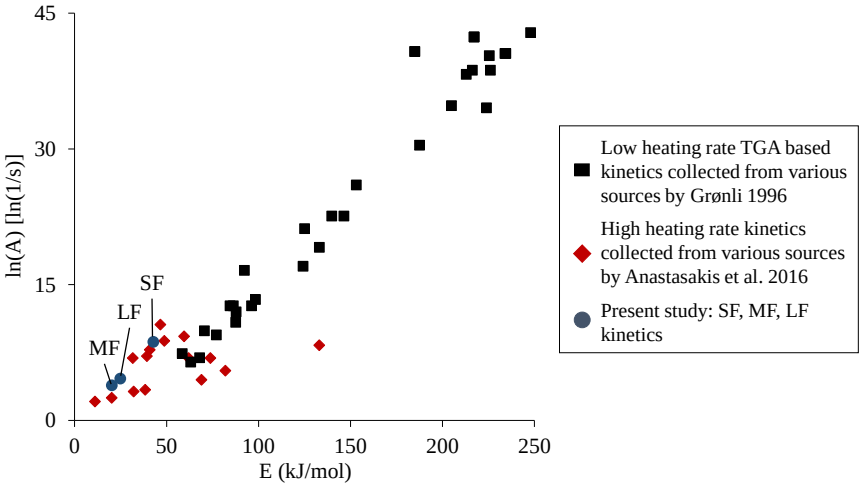

Figure 10: Comparison of low and high heating rate kinetics for various biomass materials and pure lignocellulosic components. The low heating rate kinetics are collected from various sources by Gronli in [29]. The high heating rate kinetics are collected from various sources by Anastasakis et al. in [14].

Fig. 10 compares the low and high heating rate kinetics for various biomass materials. As shown in the figure, the SF, MF and LF kinetics

are scattered at the high heating rate region, thus the results are well in line with the previous studies. The kinetics add to the limited high heating rate data available for woody biomass, and can possibly help to understand the relation between heating rate and devolatilization kinetics.

It is expected that in large scale CFD simulations where a rapid fuel heat up occurs, the kinetic parameters obtained in this work can provide more realistic mass loss results compared to the traditional low heating rate TGA kinetics. However, it is not fully clear how the obtained kinetics function at even higher heating rates, such as in pulverized fuel combustion. Furthermore, there is a lack of a comprehensive study which would show the effect of the kinetic parameters on the overall solution of a large scale CFD simulation, for example on the predicted flame characteristics or unburned fuel at the combustion chamber outlet. This kind of study would point out the significance of accurate kinetic parameter determination.

6. Conclusions and Future Work

The accurate temperature-time histories of devolatilizing fuel particles are essential in high heating rate kinetic modeling because of the exponential dependency between the reaction rate and the particle temperature. This work presents an optimization approach for determining the high heating rate biomass devolatilization kinetics. The presented approach combines experimental Drop-Tube Reactor (DTR) measurements and numerical CFD modeling. The work demonstrates that the CFD based approach accurately characterizes the external particle conditions and particle residence times, which together determine the temperature-time histories of the fuel particles.

It is shown that the non-spherical drag law of Haider and Levenspiel [24] is a suitable model for elongated biomass particles, whereas the spherical drag law is incapable of producing the experimental velocity profiles. A value of $\phi = 0.25$ for the shape factor of the non-spherical drag law is found suitable for the studied biomass particles. It is expected that the experimentally validated shape factor can provide accuracy in particle trajectory calculations in large scale CFD simulations. The suitability of the drag law should be validated for turbulent flow conditions in future studies.

The optimization approach is used for determining the Single First Order Reaction (SFOR) kinetics for woody biomass. The particles are simplified as isothermal spheres in order to maintain compatibility with the single particle models available in the commercial CFD programs. The optimization is conducted separately for three particle size groups: small, medium and large fractions. The optimized kinetic parameters are $A_{SF} = 5880$ 1/s

and $E_{SF} = 42720$ J/mol, $A_{MF} = 48.1$ 1/s and $E_{MF} = 20212$ J/mol, and $A_{LF} = 102$ 1/s and $E_{LF} = 24784$ J/mol. It is recommended that the same specific heat capacity that was used in the optimization ($c_p = 1500$ J/kgK) is used together with these parameters. In future studies, the presented approach can be applied with more sophisticated devolatilization and heat transfer models to better study the physical and chemical phenomena of the devolatilization process.

The kinetics of the medium and large particles result in almost identical mass loss profiles, while the small particle kinetics predict a significantly faster devolatilization. It is proposed that the MF/LF kinetics have compensated the internal heat transfer resistance which is neglected in the isothermal simplification, and this possibly explains the difference between the SF and MF/LF kinetics. Because of the compensation effect, it is expected that the MF/LF kinetics can predict the conversion profiles of the large particles without need for modifications to the default isothermal heat transfer model. The SF kinetics can be used separately for the small particles and either of the MF/LF kinetics for the large wood particles in large scale CFD simulations, enabling more accurate results for the whole size distribution of the fuel.

The optimized kinetics are compared with various biomass kinetics obtained from low and high heating rate studies. The results are in accordance with the other high heating rate results, as a significantly lower activation energy is obtained when compared to the low heating rate TGA based kinetics. The increase in the heating rate evidently lowers the global activation energy of the devolatilization reactions, but the mechanism which causes this effect is not clear and is a recommended subject for the future research.

Acknowledgments

The work was carried out in the Sustainable Bioenergy Solutions for Tomorrow (BEST) research program coordinated by CLIC Innovation with funding from the Finnish Funding Agency for Innovation, Tekes. The work was conducted in co-operation, and with financial support, from Valmet Technologies Oy. The contribution of all associates is gratefully acknowledged.

References

[1] I. Adeyemi, I. Janajreh, T. Arink, C. Ghenai, Gasification behavior of coal and woody biomass: Validation and parametri-

cal study, Applied Energy (In Press) (2016), ISSN: 0306-2619, doi:10.1016/j.apenergy.2016.05.119, URL: http://dx.doi.org/10.1016/j.apenergy.2016.05.119

[2] W. H. Chen, C. J. Chen, C. I. Hung, C.H. Shen, H. W. Hsu, A comparison of gasification phenomena among raw biomass, torrefied biomass and coal in an entrained flow reactor, Applied Energy 112 (2013) 421-430, ISSN: 0306-2619, doi:10.1016/j.apenergy.2013.01.034, URL: http://dx.doi.org/10.1016/j.apenergy.2013.01.034

[3] S. Xiu, N. Wang, W. Yi, B. Li, G. Shahbazi, Validation of kinetic parameter values for prediction of pyrolysis behaviour of corn stalks in a horizontal entrained-flow reactor, Biosystems Engineering 100 (2008) 79-85, ISSN: 5137-5110, doi:10.1016/j.biosystemseng.2008.01.006, URL: http://dx.doi.org/10.1016/j.biosystemseng.2008.01.006

[4] K. Papadikis, S. Gu, A. W. Bridgwater, H. Gerhauser, Application of CFD to model fast pyrolysis of biomass, Fuel Processing Technology 90 (2009) 504-512, ISSN: 0378-3820, doi:10.1016/j.fuproc.2009.01.010, URL: http://dx.doi.org/10.1016/j.fuproc.2009.01.010

[5] A. A. Bhuiyan, J. Naser, CFD modelling of co-firing of biomass with coal under oxy-fuel combustion in a large scale power plant, Fuel 159 (2015) 150-168, ISSN: 0016-2361, doi:10.1016/j.fuel.2015.06.058, URL: http://dx.doi.org/10.1016/j.fuel.2015.06.058

[6] S. R. Gubba, D. B. Ingham, K. J. Larsen, L. Ma, M. Pourkashanian, H. Z. Tan, A. Williams, H. Zhou, Numerical modelling of the co-firing of pulverized coal and straw in a 300 MWe tangentially fired boiler, Fuel Processing Technology 104 (2012) 181-188, ISSN: 0378-3820, doi:10.1016/j.fuproc.2012.05.011, URL: http://dx.doi.org/10.1016/j.fuproc.2012.05.011

[7] C. Yin, L. Rosendahl, S. K. Kær, Towards a better understanding of biomass suspension co-firing impacts via investigating a coal flame and a biomass flame in a swirl-stabilized burner flow reactor under same conditions, Fuel Processing Technology 98 (2012) 65-73, ISSN: 0378-3820, doi:10.1016/j.fuproc.2012.01.024, URL: http://dx.doi.org/10.1016/j.fuproc.2012.01.024

[8] J. Cai, W. Wu, R. Liu, An overview of distributed activation energy model and its application in the pyrolysis of lignocellulosic biomass,

Renewable and Sustainable Energy Reviews 36 (2014) 236-246, ISSN: 1364-0321, doi:10.1016/j.rser.2014.04.052, URL: http://dx.doi.org/10.1016/j.rser.2014.04.052

[9] ANSYS FLUENT, Release 14.5, Ansys Inc., Canonsburg, Pennsylvania, United States, 2012

[10] S. Zellagui, C. Schönnenbeck, N. Zouaoui-Mahzoul, G. Leyssens, O. Authier, E. Thunin, L. Porcheron, J. F. Brilhac, Pyrolysis of coal and woody biomass under N_2 and CO_2 atmospheres using a drop tube furnace - experimental study and kinetic modeling, Fuel Processing Technology 148 (2016) 99-109, ISSN: 0378-3820, doi:10.1016/j.fuproc.2016.02.007, URL: http://dx.doi.org/10.1016/j.fuproc.2016.02.007

[11] X. Shuangning, L. Zhihe, L. Baoming, Y. Weiming, B. Xueyuan, Devolatilization characteristics of biomass at flash heating rate, Fuel 85 (5) (2006) 664-670, ISSN: 0360-5442, ISSN: 0016-2361, doi:10.1016/j.fuel.2005.08.044, URL: http://dx.doi.org/10.1016/j.fuel.2005.08.044

[12] S. Jiménez, P. Remacha, J. C. Ballesteros, A. Giménez, J. Ballester, Kinetics of devolatilization and oxidation of a pulverized biomass in an entrained flow reactor under realistic combustion conditions, Combustion and Flame 152 (2008) 588-603, ISSN: 0010-2180, doi:10.1016/j.combustame.2007.10.001, URL: http://dx.doi.org/10.1016/j.combustame.2007.10.001

[13] A. Sharma, V. Pareek, D. Zhang, Biomass pyrolysis - A review of modelling, process parameters and catalytic studies, Renewable and Sustainable Energy Reviews 50 (2015) 1081-1096, ISSN: 1364-0321, doi:10.1016/j.rser.2015.04.193, URL: http://dx.doi.org/10.1016/j.rser.2015.04.193

[14] K. Anastasakis, I. Kitsiou, W. de Jong, Fast devolatilization characteristics of low cost biomass fuels, wood and reed. Potential feedstock for gasification, Fuel Processing Technology 142 (2016) 157-166, ISSN: 0378-3820, doi:10.1016/j.fuproc.2015.10.018, URL: http://dx.doi.org/10.1016/j.fuproc.2015.10.018

[15] M. Simone, E. Biagini, C. Galletti, L. Tognotti, Evaluation of global biomass devolatilization kinetics in a drop tube reactor with CFD

aided experiments, Fuel 88 (10) (2009) 1818-1827, ISSN: 0016-2361, doi:10.1016/j.fuel.2009.04.032, URL: http://dx.doi.org/10.1016/j.fuel.2009.04.032

[16] J. M. Johansen, R. Gadsbøll, J. Thomsen, P. A. Jensen, P. Glarborg, P. Ek, N. De Martini, M. Mancini, R. Weber, R. E. Mitchell, Devolatilization kinetics of woody biomass at short residence times and high heating rates and peak temperatures, Applied Energy 162 (2016) 245-256, ISSN: 0306-2619, doi:10.1016/j.apenergy.2015.09.091, URL: http://dx.doi.org/10.1016/j.apenergy.2015.09.091

[17] MATLAB, Release 2015a, The MathWorks Inc., Natick, Massachusetts, United States, 2015

[18] H. Tolvanen, L. Kokko, R. Raiko, Fast pyrolysis of coal, peat, and torrefied wood: Mass loss study with a drop-tube reactor, particle geometry analysis, and kinetics modeling, Fuel 111 (2013) 148-156, ISSN: 0016-2361, doi:10.1016/j.fuel.2013.04.030, URL: http://dx.doi.org/10.1016/j.fuel.2013.04.030

[19] H. Tolvanen, Advanced solid fuel characterization for reactivity and physical property comparison, Doctoral Dissertation, Tampere University of Technology, Publication Vol. 1359, 2016, 66 p., URL: http://URN.fi/URN:ISBN:978-952-15-3674-8

[20] H. Tolvanen, T. Keipi, R. Raiko, A study on raw, torrefied, and steam-exploded wood: Fine grinding, drop-tube reactor combustion tests in N_2/O_2 and CO_2/O_2 atmospheres, particle geometry analysis, and numerical kinetics modeling, Fuel 176 (2016) 153-164, ISSN: 0016-2361, doi:10.1016/j.fuel.2016.02.071, URL: http://dx.doi.org/10.1016/j.fuel.2016.02.071

[21] J. Ballester, S. Jiménez, Kinetic parameters for the oxidation of pulverized coal as measured from drop tube tests, Combustion and Flame 142 (3) (2005) 210-222, ISSN: 0010-2180, doi:10.1016/j.combustflame.2005.03.007, URL: http://dx.doi.org/10.1016/j.combustflame.2005.03.007

[22] N. Niemelä, Computational fluid dynamics modeling of pulverized biomass combustion using optimized reactivity parameters, Master's thesis, Tampere University of Technology, 2016, 114 p., URL: http://URN.fi/URN:NBN:fi:tty-201603223739

[23] ANSYS FLUENT, FLUENT Theory Guide, Release 14.5, Ansys Inc., Canonsburg, Pennsylvania, United States, 2012

[24] A. Haider, O. Levenspiel, Drag coefficient and terminal velocity of spherical and nonspherical particles, Powder Technology 58 (1989) 63-70, ISSN: 0032-5910, doi:10.1016/0032-5910(89)80008-7, URL: http://dx.doi.org/10.1016/0032-5910(89)80008-7

[25] W. E. Ranz, W. R. Marshall Jr., Evaporation from Drops: Part I, Chemical Engineering Progress 48 (3) (1952) 141-146

[26] J. M. Johansen, P. A. Jensen, P. Glarborg, M. Mancini, R. Weber, R. E. Mitchell, Extension of apparent devolatilization kinetics from thermally thin to thermally thick particles in zero dimensions for woody biomass, Energy 95 (2016) 279-290, ISSN: 0360-5442, doi:10.1016/j.energy.2015.11.025, URL: http://dx.doi.org/10.1016/j.energy.2015.11.025

[27] J. C. Lagarias, J. A. Reeds, M. H. Wright, P. E. Wright, Convergence properties of the Nelder-Mead simplex method in low dimensions, SIAM Journal of Optimization 9 (1) (1998) 112-147, ISSN: 1095-7189, doi:10.1137/S1052623496303470, URL: http://dx.doi.org/10.1137/S1052623496303470

[28] M. Asadullah, S. Zhang, C. Z. Li, Evaluation of structural features of chars from pyrolysis of biomass of different particle sizes, Fuel Processing Technology 91 (8) (2010) 877-881, ISSN: 0378-3820, doi:10.1016/j.fuproc.2009.08.008, URL: http://dx.doi.org/10.1016/j.fuproc.2009.08.008

[29] M. Gronli, A theoretical and experimental study of the thermal conversion of biomass, Doctoral dissertation, Norwegian University of Science and Technology, 1996, 282 p.